



HAL
open science

Wind/WAVES Observations of Auroral Kilometric Radiation: Automated Burst Detection and Terrestrial Solar Wind - Magnetosphere Coupling Effects

A. R. Fogg, C. M. Jackman, J. E. Waters, X. Bonnin, L. Lamy, B. Cecconi, K. Issautier, C. K. Louis

► To cite this version:

A. R. Fogg, C. M. Jackman, J. E. Waters, X. Bonnin, L. Lamy, et al.. Wind/WAVES Observations of Auroral Kilometric Radiation: Automated Burst Detection and Terrestrial Solar Wind - Magnetosphere Coupling Effects. *Journal of Geophysical Research Space Physics*, 2022, 127, 10.1029/2021JA030209 . insu-03713304

HAL Id: insu-03713304

<https://insu.hal.science/insu-03713304>

Submitted on 4 Jul 2022

HAL is a multi-disciplinary open access archive for the deposit and dissemination of scientific research documents, whether they are published or not. The documents may come from teaching and research institutions in France or abroad, or from public or private research centers.

L'archive ouverte pluridisciplinaire **HAL**, est destinée au dépôt et à la diffusion de documents scientifiques de niveau recherche, publiés ou non, émanant des établissements d'enseignement et de recherche français ou étrangers, des laboratoires publics ou privés.



Distributed under a Creative Commons Attribution 4.0 International License

JGR Space Physics



RESEARCH ARTICLE

10.1029/2021JA030209

Key Points:

- A novel technique has been developed to detect individual Auroral Kilometric Radiation bursts in Wind/WAVES data
- When the technique is applied to 2000–2004 data, about 5000 bursts are detected with median duration 30–60 min
- During burst windows, higher solar wind velocity, more negative IMF B_z and greater geomagnetic activity is observed

Correspondence to:









A. R. Fogg,
arfogg@cp.dias.ie

Citation:

Fogg, A. R., Jackman, C. M., Waters, J. E., Bonnin, X., Lamy, L., Cecconi, B., et al. (2022). Wind/WAVES observations of Auroral Kilometric Radiation: Automated burst detection and terrestrial solar wind - magnetosphere coupling effects. *Journal of Geophysical Research: Space Physics*, 127, e2021JA030209. <https://doi.org/10.1029/2021JA030209>

Received 10 DEC 2021
Accepted 4 APR 2022

Wind/WAVES Observations of Auroral Kilometric Radiation: Automated Burst Detection and Terrestrial Solar Wind - Magnetosphere Coupling Effects

A. R. Fogg¹ , C. M. Jackman¹ , J. E. Waters² , X. Bonnin³ , L. Lamy^{3,4} ,
B. Cecconi³ , K. Issautier³ , and C. K. Louis¹ 

¹School of Cosmic Physics, DIAS Dunsink Observatory, Dublin Institute for Advanced Studies, Dublin 15, Ireland, ²Space Environment Physics Group, School of Physics and Astronomy, University of Southampton, Southampton, UK, ³LESIA, Observatoire de Paris, Université PSL, CNRS, Sorbonne Université, Université de Paris, Meudon, France, ⁴CNRS, CNES, LAM, Pythéas, Aix Marseille Université, Marseille, France

Abstract Auroral Kilometric Radiation (AKR) is the strongest terrestrial radio emission, and emanates from the same electron acceleration regions from which particles precipitate into the ionosphere, exciting the aurorae and other phenomena. As such, AKR is a barometer for the state of solar wind - magnetosphere - ionosphere coupling. AKR is anisotropically beamed in a hollow cone from a source region generally found at nightside local times, meaning that a single source region cannot be viewed from all local times in the magnetosphere. In radio data such as dynamic spectra, AKR is frequently observed simultaneously to other radio emissions which can have a similar intensity and frequency range, making it difficult to automatically detect. Building on a previously published pipeline to extract AKR emissions from Wind/WAVES data, in this paper a novel automated AKR burst detection technique is presented and applied to Wind/WAVES data. Over a five year interval, about 5000 AKR bursts are detected with median burst length ranging from about 30 to 60 min. During detected burst windows, higher solar wind velocity is observed, and the interplanetary magnetic field clock angle is observed to tend toward $B_z < 0$, $B_y < 0$, when compared with the entire statistical interval. Additionally, higher geomagnetic activity is observed during burst windows at polar, high and equatorial latitudes.

Plain Language Summary Auroral Kilometric Radiation (AKR) is a terrestrial radio emission which is excited by the same electrons which enhance the aurorae. Due to a combination of complex beaming, and the statistical position of the source region, an AKR event cannot be observed at all positions in the Earth's magnetosphere. A combination of different radio emissions are simultaneously observed in the radio data, including both AKR and non-AKR sources. Building on previous work, in this paper individual AKR burst events are automatically detected from Wind/WAVES data over a five year interval. About 5000 events are detected over the interval, during which the observed geomagnetic activity was higher. Higher solar wind velocity and differences in the morphology of the interplanetary magnetic field are also observed during burst windows, both of which are known to excite magnetospheric dynamics.

1. Introduction

Auroral kilometric radiation (AKR) is a terrestrial radio emission broadly observed between 30 and 800 kHz, which is excited by the same electron acceleration regions which excite its namesake, the aurora (Benson & Calvert, 1979; Benson et al., 1980; Green & Gurnett, 1979; Gurnett, 1974; Huff et al., 1988). First observed in the 1960s (Dunckel et al., 1970), AKR is the dominant terrestrial radio emission, and its main band generally appears between 100 and 400 kHz, with powers up to 10^9 W (e.g., Gurnett, 1974; Zhao et al., 2019) and maximum intensity typically observed at around 200 kHz (Gurnett, 1974). Since then, AKR has been systematically observed with radio and plasma wave instruments on board spacecraft such as IMP 6 and 8, Hawkeye, Wind, GEOTAIL, POLAR, IMAGE, the Cluster array and Cassini (e.g., Desch et al., 1996; Gallagher & D'Angelo, 1981; Green et al., 1977, 2003; Gurnett, 1974; Hashimoto et al., 1998; Kasaba et al., 1997; Kurth et al., 1998; Lamy et al., 2010; Mutel et al., 2008; Voots et al., 1977; Waters, Jackman, et al., 2021). As an indicator of magnetic disturbance, AKR has been shown to be well correlated with the Auroral Electrojet (AE) index (Dunckel et al., 1970; Gurnett, 1974; Voots et al., 1977), and as such AKR observations allude to solar wind -

© 2022. The Authors.

This is an open access article under the terms of the [Creative Commons Attribution License](https://creativecommons.org/licenses/by/4.0/), which permits use, distribution and reproduction in any medium, provided the original work is properly cited.

magnetosphere - ionosphere coupling (Gallagher & D'Angelo, 1981; Zhao et al., 2019) and can be well correlated with substorm activity (e.g., Morioka et al., 2011).

The AKR source region is found to be within the auroral plasma cavity, a region with low plasma density, around 1 cm^{-3} (Calvert, 1981b; Ergun et al., 1998; Hilgers, 1992; Johnson et al., 2001), and precipitating energetic electrons present (Ergun et al., 1998; Green & Gurnett, 1979). Centered on about 70° invariant latitude (Calvert, 1981b; Johnson et al., 2001), the cavity region can extend between 30 and 300 km in latitude (Ergun et al., 1998), and between 1.8 Earth radii (R_E , $1R_E \approx 6,371 \text{ km}$) and $3R_E$ in the radial direction (Calvert, 1981b). Auroral acceleration regions house energetic electrons which are accelerated down magnetic field lines, perhaps by a dipolarisation of the tail magnetic field following magnetic reconnection, toward their roots in the polar ionosphere. Depending on the angle between their velocity vector and the converging polar magnetic field, they may reflect at the magnetic mirror points or precipitate into the ionosphere, exciting, among other phenomena, the aurora. Following reflection at the magnetic mirror point, electrons travel up along magnetic field lines until they reach a region of low plasma density, often termed the plasma cavity or trough (e.g., Benson & Calvert, 1979; Calvert, 1981b; Ergun et al., 1998; Mutel et al., 2008). In this region, there is not enough plasma to contain the energy of the incoming energetic electrons (e.g., Treumann & Baumjohann, 2020), and so the electrons undergo wave-particle interactions at a frequency close to the electron cyclotron frequency. Termed the *Electron-Cyclotron Maser Instability* (ECMI), the particles emit their energy in the form of circularly polarised radio emission, in the terrestrial case AKR. Along with these field aligned energetic electrons, particles with a range of different pitch angles exist within the plasma cavity and similarly contribute to the instability.

The local time (LT), depth (in density) and altitude extent of the plasma cavity vary with geomagnetic activity, the degree of solar illumination of the ionosphere (and hence season), and movement of the polar cap boundary (Janhunen et al., 2002; Johnson et al., 2001). AKR source regions have been detected at all LTs (e.g., Mutel et al., 2004), but are more often observed in the nightside region. Due to its production by the ECMI, the altitude of the radio source is expected to be inversely proportional to the frequency of the observed radio emission. Previous work included the proposal that dual AKR source regions may exist at substorm onset (Morioka et al., 2007). First, a low altitude (high frequency) source related to inverted-V particle acceleration, appearing in substorm growth phase around 4,000–5,000 km altitude. At substorm onset a second, high altitude (low frequency), source appears between 6,000 and 12,000 km altitude relating to either local field-aligned or Alfvénic acceleration.

ECMI theory predicts that AKR is anisotropically beamed in a hollow cone at angles near perpendicular to a source region centered on a magnetic field line (Wu, 1985; Wu & Lee, 1979). Gurnett (1974) noted that there was a cone shaped nature to the statistical pattern of AKR observations, later described as a solid cone by Green et al. (1977); Green and Gallagher (1985) and a hollow cone by Calvert (1981a). Recently, Mutel et al. (2008) combined data from the four Cluster spacecraft to examine the beaming of AKR, concluding that the beaming is confined to a plane of finite width containing the magnetic field vector, which is tangent to the source magnetic latitude circle, confirming previous modeling work by Louarn and Le Quéau (1996); Pritchett et al. (2002). Observations also highlight how geomagnetic activity can disturb the illumination pattern of AKR, reaching lower latitudes near midnight LT for higher K_p (e.g., Kasaba et al., 1997).

AKR source regions in both hemispheres produce hollow cones of circularly polarised emission with mostly right-handed from the northern magnetic (southern geographic) hemisphere, and left-handed from the southern magnetic (northern geographic) hemisphere (Kaiser et al., 1978). Combined with plasmaspheric refraction effects as the beam passes from the plasma cavity to the surrounding denser plasma (Mutel et al., 2008; Xiao et al., 2007), this anisotropic beaming provides challenges for observing AKR. For a hypothetical source region fixed in latitude and local time that is continuously emitting AKR, a moving spacecraft will transit into and out of its illumination region as it orbits the Earth. At equatorial latitudes near midnight LT inside about $12R_E$, the spacecraft falls into the statistical equatorial shadow zone (e.g., Gallagher & Gurnett, 1979), seeing neither hemisphere's AKR emission cone. At greater radial distances, the spacecraft will see a combination of both hemisphere's AKR emission around the equator (distinguishable only by their polarisation), but at high latitudes may fall into the illumination region of one hemisphere or the other (Hashimoto et al., 1998).

Although it can be observed at any local time (Zhao et al., 2019), AKR is most often viewed in the midnight/evening sector between 18 and 6 LT (e.g., Green et al., 1977; Gurnett, 1974; Kasaba et al., 1997; Zhao et al., 2019). Further to the LT constraints on viewing, a 24 hr modulation of the AKR signal has been identified by Lamy

et al. (2010); Panchenko et al. (2009); Morioka et al. (2013) relating to the diurnal precession of the tilted dipole magnetic field. Finally, the observed power of the emission drops off as $\frac{1}{R^2}$ (Green et al., 1977; Gurnett, 1974), so observers closer to the source region receive higher power emission than a spacecraft in the distant magnetotail.

Additionally, decades of observation of AKR have highlighted its variability relating to the geomagnetic activity. In particular, the intensity and frequency range of AKR has been shown to relate to the geomagnetic indices AE (Dunckel et al., 1970; Hashimoto et al., 1998; Voots et al., 1977) and Kp (Kasaba et al., 1997), showing strong links to geomagnetic activity. Increased geomagnetic activity results in intensifications in AKR and longitudinal extensions of the source region, which enables AKR viewing on the dayside (Zhao et al., 2019). Enhancements in AKR intensity are concurrent with auroral brightenings (Gurnett, 1974), which observations suggest depend strongly on solar wind and Interplanetary Magnetic Field (IMF) coupling. Finally, AKR can excite electrons in the radiation belts, posing potential dangers to spacecraft in the near-Earth environment (Zhao et al., 2019, and references therein).

The strength and direction of the IMF and solar wind variability are well known to influence the transfer of energy into the terrestrial system, and as a part of the solar wind coupled magnetosphere, AKR is no different. Gallagher and D'Angelo (1981) showed a correlation between the solar wind flow speed and the log of AKR intensity, and that enhanced intensity was observed under IMF B_y conditions. Similarly, Desch et al. (1996) showed that peaks in solar wind flow speed coincide with low frequency extensions (LFEs) in radio emission, and again, that this appears preferentially when there is a B_y component to the IMF. Additionally, Saturn Kilometric Radiation (SKR), which is generally considered analogous to AKR, has been shown to respond to changes in solar wind dynamic pressure (Desch, 1982; Desch & Rucker, 1983; Jackman et al., 2010; Taubenschuss et al., 2006). Furthermore, Kurth et al. (1998) examined radio spectra and AKR intensity during the passing of a magnetic cloud event, and showed that prolonged southward IMF B_z excited AKR emission, as did a rapid solar wind pressure enhancement which triggered substorm activity. Finally, increased ionospheric densities relating to season and/or solar cycle reduce the altitude range of the plasma cavity, affecting the frequency of emission, and cause higher plasma densities in the cavity, resulting in less intense AKR (Green et al., 2003).

In this study, a novel technique to automatically detect individual AKR burst events is presented and applied to the Wind/WAVES data set from 2000 to 2004 when the viewing was most favorable for AKR detection. Solar wind, IMF and geomagnetic indices are examined during these burst windows. Section 2 describes the datasets used, Section 3 examines the LT viewing constraints on AKR, and Section 4 outlines the automated burst detection algorithm. The analysis of burst properties and their link to heliospheric conditions is shown in Sections 5 and 6 respectively, followed by concluding remarks in Section 7.

2. Data

2.1. Wind WAVES Data

The Wind satellite was launched in November 1994 as part of NASA's International Solar Terrestrial Physics Program (ISTP; e.g., Wilson III et al., 2021). Investigating energy transport in Solar Wind - Magnetosphere coupling was among the goals of the ISTP, to which Wind has contributed significantly during its multi-decadal lifetime. Wind carries a suite of instruments onboard including the WAVES instrument which is utilized in this paper (Bougeret et al., 1995). Amalgamated from some of the other instruments, Wind provides upstream solar wind plasma and interplanetary magnetic field measurements (Lepping et al., 1995; Lin et al., 1995; Ogilvie et al., 1995; Von Rosenvinge et al., 1995) to the OMNI data set (described later, King and Papitashvili (2005)), for which it is perhaps most famous in the community.

WAVES is the Radio and Plasma Wave Investigation on the Wind spacecraft, which aims to provide comprehensive observations of radio and plasma phenomena from a fraction of a Hz up to 14 MHz (Bougeret et al., 1995). WAVES is composed of three electric dipolar antenna systems, two in the spin plane and one aligned with the spin axis. The RAD1 radio receiver operates 256 frequency channels within its 20–1,040 kHz range, which encompasses the AKR range. Over each approximately three minute sweep cycle, selected frequency channels (typically 64, Waters, Jackman, et al., 2021) are sampled. For a full description of the operational modes and technical details of Wind/WAVES, the reader is directed to Bougeret et al. (1995). Level 2 (L2) data from the

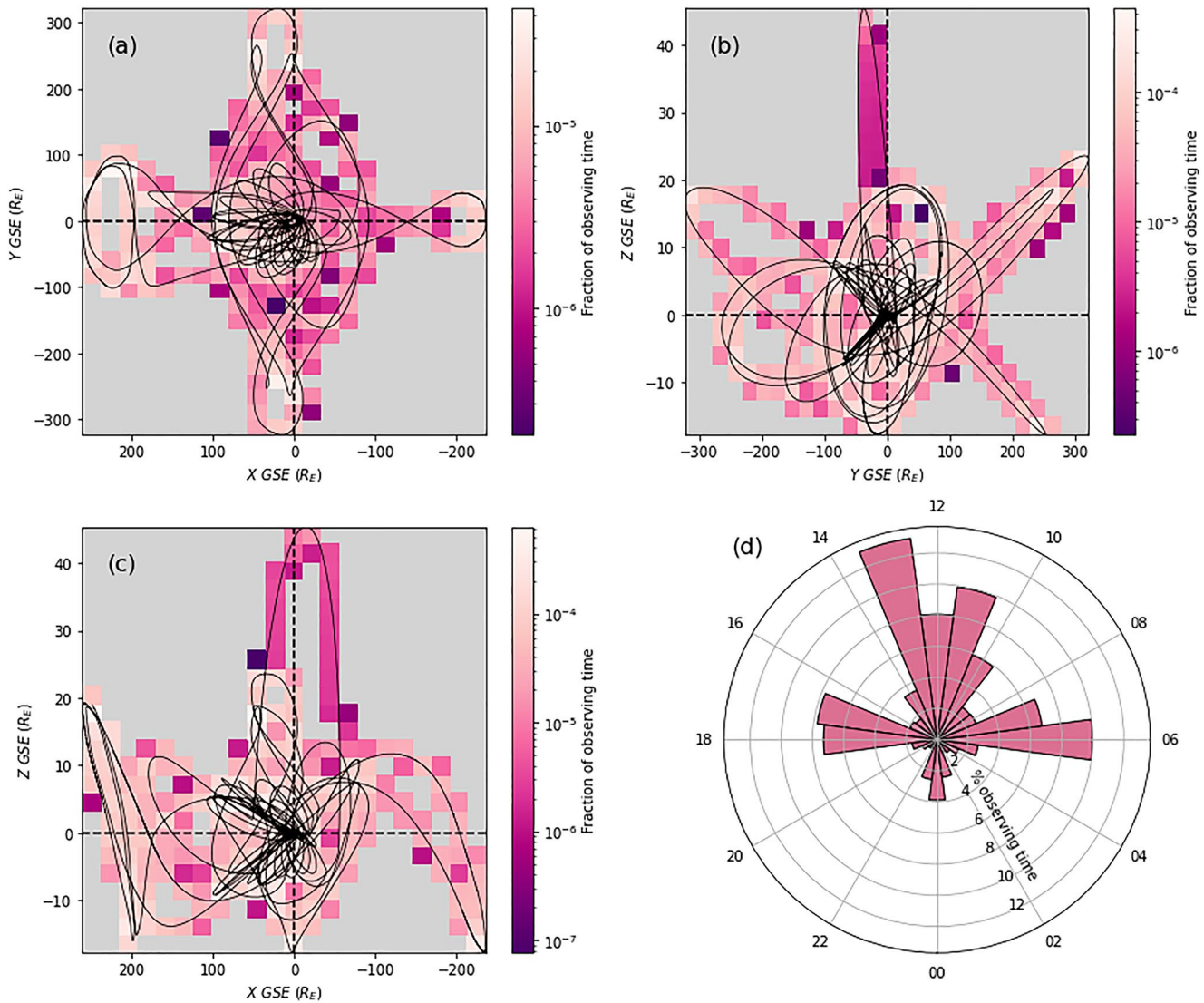


Figure 1. Wind spacecraft trajectory between 2000 and 2004 inclusive in the (a) X-Y GSE plane, (b) Y-Z GSE plane, (c) X-Z GSE plane. Trajectory is drawn in black, overlapped onto a two dimensional histogram of the fraction of observing time spent in each bin. Bin width is $25 R_E$ in X and Y, and $3 R_E$ in Z. (d) Histogram of Wind observing time in each local time sector; 1 hr width LT bins are represented by a bar with length equal to percentage of observing time, and angular position and width representing the bin position and size in LT. LT values are indicated around the edge, with noon at the top.

RAD1 receiver, containing approximately three minute resolution sweep cycles over selected frequency bands, is used to observe AKR, and normalised to 1 AU.

In its frequency range, WAVES has been able to observe a number of radio phenomena, and in particular has contributed great understanding to solar type II, III and IV radio bursts (e.g., Wilson III et al., 2021). Importantly for this study, the WAVES RAD1 receiver senses between 20 and 1,000 kHz which encapsulates the AKR spectral range, and having spent about the first decade of its lifetime in the near-Earth environment, it has recorded a wealth of AKR observations.

Wind's trajectory from 2000 to 2004 inclusive is overlapped onto a histogram showing fraction of observing time in the three different planes of Geocentric Solar Ecliptic (GSE) coordinates in Figures 1a–1c. In this period, Wind made several different orbital maneuvers, and as a result visited a variety of locations in the near-Earth environment. This meant it had a variable view of the Earth's magnetosphere, from different latitudes, local times and radial distances. Due to the anisotropic beaming of AKR emission, a given source region can only be observed

from certain local times and latitudes. Simultaneously observed emission from both hemispheres (seen near the equator) cannot be distinguished without the polarisation of the emission, which cannot be easily retrieved from Wind/WAVES/RAD1 data (Waters, Jackman, et al., 2021).

The distribution of observing time spent in each local time sector is presented in Figure 1d; one bar is plotted centered on each 1 hr width LT bin, with length representing the percentage of Wind's observing time spent in that sector. Although AKR can be observed at any LT, previous observations have shown that it is most often observed in the nightside sector between 18 and 6 LT (e.g., Green et al., 1977; Gurnett, 1974; Kasaba et al., 1997; Zhao et al., 2019) as a result of a prominent nightside emission region. In this five year interval, about 36% of time was spent in the 18-6 sector, providing approximately 1.8 years of observing time in the prime AKR observational sector, plus good observational time in the dayside sector. Positioned from near the maximum and down the trailing end of solar cycle 23, the years selected are expected to have a range of solar wind variability, including some strong solar wind driving of the magnetosphere. This broad parameter space of upstream driving will allow examination of AKR under both disturbed and quiet magnetospheric conditions.

2.2. Empirical AKR Selection Technique

Wind/WAVES is capable of sensing any radio emission in its frequency range, and so often observes a combination of emission from different sources. In Figure 2a, L2 Wind/WAVES data is presented in a frequency-time-intensity spectrogram from 1 November 2002. In this panel, a variety of different signals can be seen: AKR emission is seen between ~0930–1145 UT in the frequency range 100–400 kHz, followed by second, brighter burst of AKR beginning at ~1215 UT. Additionally, a solar type III radio burst is seen around 0900 UT extending from frequencies higher than Wind/WAVES can detect, and down to about 100 kHz (a characteristic swooping shape e.g., Wilson III et al., 2021). Finally, some low frequency but high intensity emission of local origin is seen from around 1000 UT toward the end of the presented interval. This example shows that Wind/WAVES can observe a complex mixture of radio signals, that can be simultaneously occurring over similar frequency ranges, with similar intensities.

A recently developed technique by Waters, Jackman, et al. (2021) is utilized to extract AKR emission from amongst this complex superposition of radio phenomena. Each frequency-time bin presented in the spectrogram in Figure 2a is sampled several times within the approximately three minute sweep window. These individual flux measurements are modeled as a normal distribution, centered on the mean. After normalizing the measurements by their mean, the standard deviation (σ_z) of the sample is calculated. AKR emission has a high σ_z (i.e., high temporal variability) when compared with solar emissions and the ambient background, so an empirical threshold is applied to σ_z values, keeping only data which meets the condition. This technique removes slowly varying emissions such as solar radio emissions and most of the background, resulting in the frequency-time-intensity spectrogram presented in Figure 2b (panels 2(c-e) will be described in Section 4). Hereafter referred to as W21-selected data, in this example the AKR emissions between about 100 and 400 kHz have been extracted without the solar and low frequency emissions. The Waters, Jackman, et al. (2021) technique has drastically simplified what was previously a very complex picture of simultaneous emissions from different sources crossing the same frequency bands, to leave mainly AKR emission remaining.

2.3. OMNI Data

High resolution OMNI (King & Papitashvili, 2005) data is used in this study to characterize the solar wind and IMF properties, as well as geomagnetic indices. The OMNI data set is an extensive set of observations combining data from several upstream solar wind monitors, primarily ACE and Wind, and propagated to the subsolar bow shock (Weimer et al., 2002, 2003; Weimer & King, 2008). A multi-decadal data set, OMNI also includes a number of geomagnetic indices from other sources, providing a user-friendly and comprehensive set of observations of the conditions in the near-Earth environment. In this study, solar wind, IMF and geomagnetic indices are extracted from the OMNI data set to characterize the upstream driving conditions and corresponding geomagnetic response relating to AKR burst observations. The parameters described below were obtained from through OMNIWeb: <https://omniweb.gsfc.nasa.gov/hw.html>.

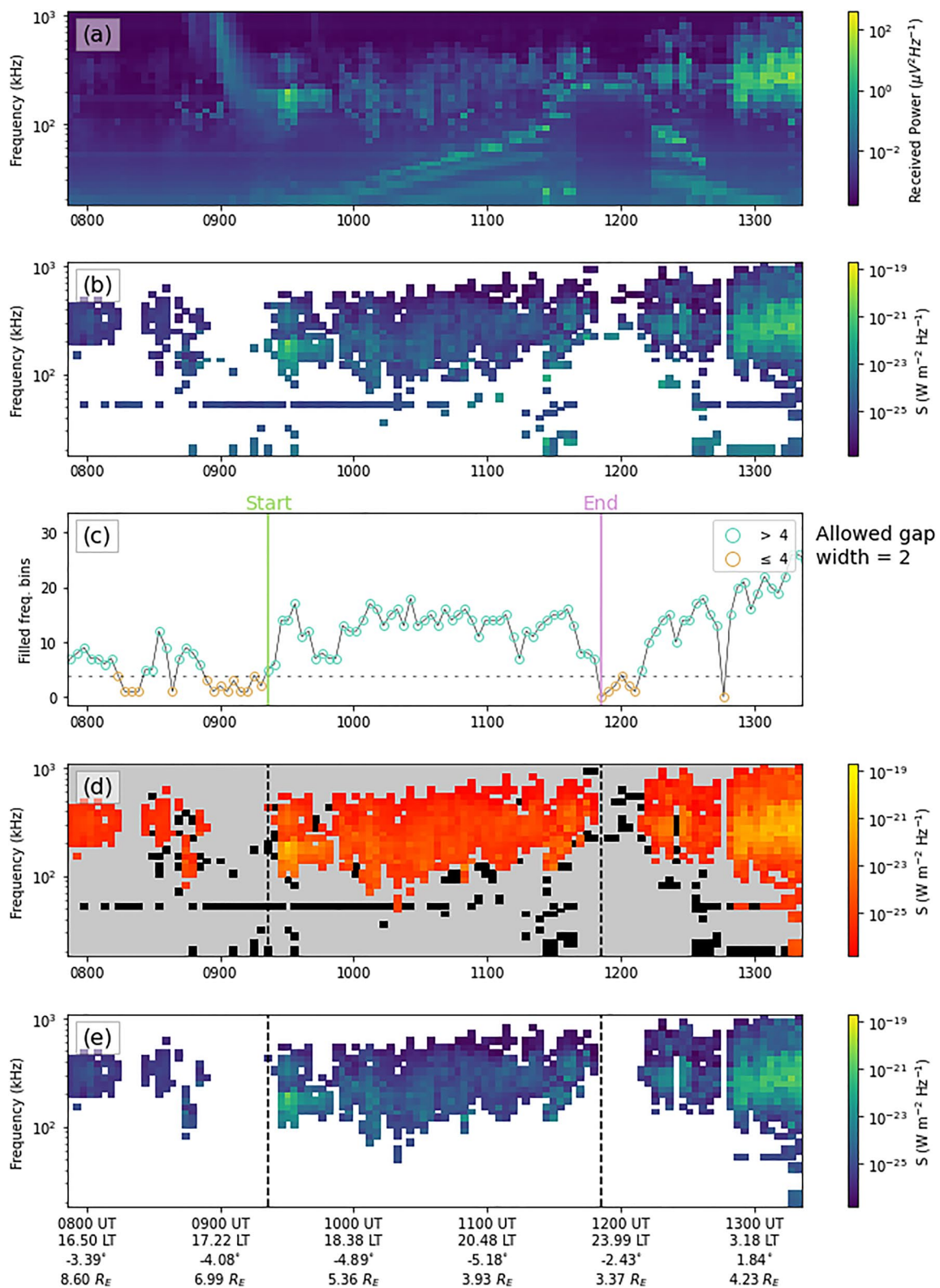


Figure 2. Frequency-time-intensity spectrograms of (a) L2 Wind/WAVES data, (b) W21-selected AKR data, (d) W21-selected AKR data, data selected in burst selection in orange-yellow, otherwise black, (e) burst selected data from 1 November 2002. Panel (c) shows the number of filled frequency bins as a function of time in W21-selected data shown in panel (b); empirical threshold of four bins is indicated and times meeting the condition are colored turquoise, otherwise orange. All intensities according to individual color bars. Tick labels on the x axis indicate universal time on panels (a)–(d), and universal time and spacecraft position in terms of local time, latitude, and radial distance in panel (e).

The interplanetary magnetic field is characterized using the IMF clock angle ($\theta_{clk} = \tan^{-1} \left(\frac{B_Y}{B_Z} \right)$), magnetic field strength ($B_T = \sqrt{B_X^2 + B_Y^2 + B_Z^2}$), and components B_Y and B_Z . θ_{clk} indicates the combination of B_Y and B_Z , both of which are known to control the dayside reconnection rate (e.g., Dungey, 1961; Grocott et al., 2003, 2004, 2008). The solar wind conditions are parameterized by its velocity (V_{SW}) and proton density (N_{SW}) which go toward the solar wind dynamic pressure ($P_{SW} \approx N_{SW} V_{SW}^2$) which pushes against the geomagnetic field to control the size of the magnetosphere, and finally the solar wind electric field ($E_{SW} \approx -V_{SW} B_Z$). The E_{SW} component depending on B_Z is selected for the analysis over the component depending on B_Y since AKR is well correlated and often driven by substorm activity, which itself is dominated by B_Z effects.

Finally, geomagnetic activity is described by the polar cap index (PC(N), Troshichev & Andrezen, 1985; Stauning, 2013), upper and lower auroral electrojet indices (AU and AL, Davis & Sugiura, 1966; World Data Center for Geomagnetism Kyoto et al., 2015), and SYM-H (Iyemori, 1990), which are derived from magnetometer stations at near polar, auroral and equatorial latitudes respectively. Each index records deflections in magnetometer data as a result of changes in overhead currents. PC(N) is an indicator of the speed of open flux across the polar cap and equivalently the strength of polar ionospheric electrodynamics. AU and AL indicate activity in the auroral zone - characteristic signatures in AL indicate substorm activity; similarly, SYM-H measures the ring current, indicating geomagnetic storms (e.g., Wanliss & Showalter, 2006).

3. Local Time Variations in AKR Power

Although AKR has been observed at all LTs, the AKR source region has been widely shown to be persistent at nightside LTs, where substorms are well known to inject large amounts of energy into the nightside ionosphere and similarly energize AKR. In order to understand AKR intensity relative to the solar wind - magnetosphere interaction, the average observed AKR power at different observing locations must first be understood. In particular, different LT regions within the magnetosphere can be dominated by very different processes, and so the relationship between the AKR intensity and observer LT is investigated here using the W21-selected AKR data.

In order to characterize the strength of AKR emission at a given time, the same approach is taken as in Waters, Jackman, et al. (2021), to integrate the W21-selected AKR data between 100 and 650 kHz. This is a slightly more conservative approach than taken by others, for example Lamy et al. (2010) who used the range 30–650 kHz. The 100–650 kHz frequency range is selected to avoid including more transient lower frequency emission. The integrated intensity, which is calculated as described in the appendices of Lamy et al. (2008), is then a measure of the strength of the observed AKR emission at a given time. For a fixed observer, a higher integrated intensity implies stronger AKR driving.

For each available observing interval of approximately three minutes in 2000–2004 inclusive, the integrated power is calculated. Each of these measurements is associated with the spacecraft LT, and binned accordingly into 0.5 hr LT bins. The median integrated power in each of these LT bins is then presented as the black curve in Figure 3a, where the color of the dot represents the relative sampling in each LT bin, and the gray shade shows the standard deviation relating of the sample in each bin. The green curve will be discussed later. Due to Wind's uneven sampling of the near-Earth environment, the amount of observations in each LT bin varies. The lowest number of observation intervals incorporated into an average is 1,181 which equates to roughly 2.5 days observation time, enough to see multiple AKR bursts. Despite this, there are high amounts of sampling at approximately midnight, dawn, noon and dusk, which will aid LT comparisons. The highest average integrated intensity is viewed at nightside LTs, with powers several orders of magnitude higher than the lowest powers seen on the dayside. The standard deviation in these averages is similar across LT.

There are also some variations in power from bin to bin, of varying magnitude, for example, between 10 and 15 LT. In order to understand the broad LT differences in power, a rolling boxcar average is performed to remove these rapid variations between neighbor bins. In Figure 3b, the black curve shows the average of measurements in each 0.5 hr LT bin and 4 bins either side (± 2 hr, noting that LT is periodic), again with colored dots showing the sampling according to the scale on the right, and the gray shade representing the standard deviation in each bin. The green curve is the same as the black curve from panel 3(a) for easy comparison (similarly, the green curve in 3(a) is the same as the black curve in 3(b)). In this smoothed version, the curve shows three distinct regions

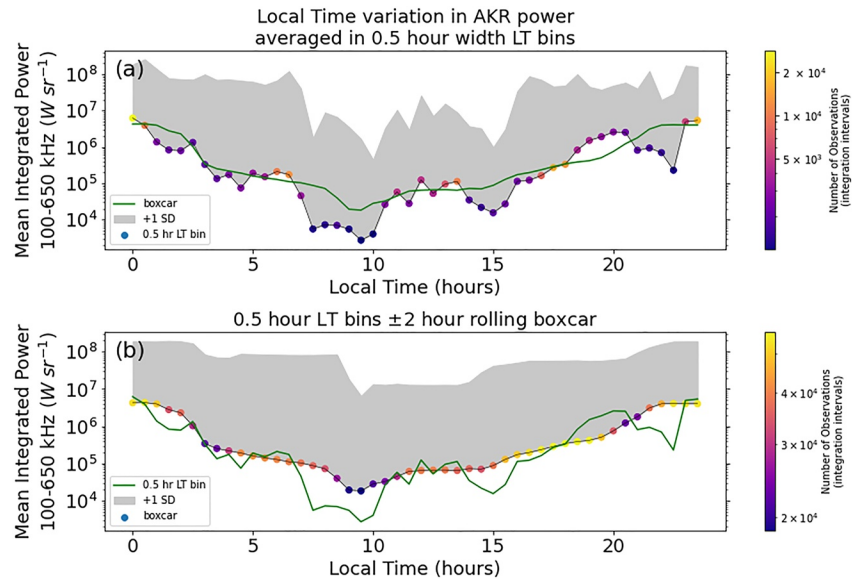


Figure 3. Median integrated power as a function of spacecraft LT for 2000–2004 W21-selected AKR data. (a) The black line is the median integrated power in 0.5 hr width LT bins centered on integer and half integer hours with colored dots indicating the number of observation integration intervals (approximately three minutes) incorporated into the average according to the scale on the right. The gray shade fills the area between the value and plus one standard deviation for each average. The green curve is the same as the black curve in the bottom panel. (b) The black line is the median integrated power for each 0.5 hr width LT bin incorporating data from two hours either side in a rolling boxcar. The color of the dot represents the number of integration intervals according to the color scale, and the gray shade the standard deviation for each average. The green curve is the same as the black curve in the top panel.

of different levels of integrated power. At midnight (21–3 LT), the median value for this curve is $3.3 \times 10^6 \text{ W sr}^{-1}$, whereas at dawn (3–9 LT) and dusk (15–21 LT) the mean values are $2.0 \times 10^5 \text{ W sr}^{-1}$ and $4.0 \times 10^5 \text{ W sr}^{-1}$ respectively, an order of magnitude less intense. At noon (9–15 LT), the AKR is a further order of magnitude less intense, with a mean value of $5.0 \times 10^4 \text{ W sr}^{-1}$.

There is a large variation in the average observed intensity at different observing LTs, which results from the convolution of the strongly anisotropic AKR beaming with the time variable longitudinal extent of the source region. Observations of integrated intensity will then be a superposition of the LT viewing constraints, as well as the solar wind - magnetosphere coupling which is the desired investigation in this paper. In order to disentangle the difference between the two, the smoothed LT-intensity variation (black curve Figure 3b) will be used to represent intensity measurements as a ‘fraction’ above the LT average - thereby values above one are enhanced above the usual, and less than one are weaker than usual.

4. Automatic Detection of AKR Bursts

In this section, the automated burst detection algorithm will be described in detail. An example of an automatically detected AKR burst is presented in Figure 2, showing the stages of processing from L2 (panel 2(a)) through to individual burst events (panel 2(e)). The burst detection algorithm consists of the detection of burst start and end, and the upper and lower frequency limits at each time during the burst. Identification of burst start time allows analysis of coupling timescales between the solar wind at the subsolar point and the (mostly) nightside electron acceleration processes driving AKR. Additionally, the evolution of the upper and lower frequency limits during burst time will allow analysis of AKR morphology and source location changes relating upstream solar wind driving.

First, the Waters AKR selection technique is run on the data, as described in Section 2.2, which extracts the AKR emission from amongst other radio emissions in panel 2(a), resulting in the W21-selected data presented in panel 2(b). This W21-selected AKR data is comprised of frequency-time bins which are either ‘filled’ with

an intensity measurement, or not. In the example presented in Figure 2b, the AKR bursts are seen as coherent clusters of filled bins. There are also sparse individual filled bins or ‘salt and pepper’ noise, some small patches of elevated intensity emission at low frequencies, and persistent Radio Frequency Interference (RFI) at 52 kHz. In order to separate the AKR burst from amongst these other emissions, the burst search algorithm seeks to identify clusters of bins which contain a flux measurement, relying on the spatially distinct nature of the AKR bursts in frequency-time space.

At each integration time, the number of filled frequency bins is counted, presented in panel 2(c) for the example burst. The start of the burst is detected as the first instance where a user-defined threshold number of bins is met for a minimum number of intervals. The threshold number of bins was optimized empirically by examining different burst morphologies and sizes. Defining a minimum number of intervals for the threshold to be met essentially defines a minimum burst length - this step was essential to prevent detection of sparse, short lived signals. A minimum length of 4 time steps was chosen as this is approximately equal to 12 min, around the timescale of a short lived substorm or *pseudo-breakup* (e.g., Yeoman et al., 2000). This burst start time is recorded.

Next, the algorithm searches for the end of the burst, where the number of filled bins falls below the threshold. Short intervals, of at most one time step, where the number of filled bins drops below the threshold are allowed, to account both for instrument outages, and temporary narrowing of burst morphology. There is no limit to the number of these short outages that is allowed, as multiple instrument outages could occur during a long duration burst. The burst end is detected as the first drop below the threshold (4 filled bins) longer than one time interval following the burst onset. Outages in the number of filled bins are limited in length as a long outage in available frequency bins is indistinguishable from there being no data.

Between the detected burst start and end time, the upper and lower frequency limits are determined next. This further refines the burst definition, removing any of the emissions within the burst window which are not part of the cluster. This also enables statistical comparison of burst morphology, and the temporal evolution of the frequency range of the burst. At a single time step within the burst window, the packing density (percentage of frequency bins that contain an intensity measurement) between all possible combinations of lower and upper frequency is calculated. The combination of lower and upper frequency limits within which the packing density equals or exceeds the empirically selected threshold of 80% is selected. If multiple windows meet the threshold, the widest is selected so that the burst is not unnecessarily narrowed. For example, for a burst with 10 consecutive frequency bins filled, numbered 0-9, the packing density will meet the threshold for any combination of these frequency limits. The widest (0-9) contains all the data, any narrower and some of the region meeting the empirical criterion is excluded. Additionally, if no combination of upper and lower frequency limits is found (e.g., in an allowed data gap), then the limits are the same as the previous time step. This technique is repeated at each time interval in during the burst window. In panel 2(d), the data selected by this technique is colored according to the orange-yellow color scale, and that which is excluded is colored black. For this example burst between the labeled start and end time, the low frequency emission, RFI band, and other ‘salt and pepper’ noise have been excluded by the selection technique.

Combining both the burst start and end time detection, and the lower and upper frequency limits, the remaining selected data is presented in panel 2(e). In this complex interval, AKR emission has been initially selected from amongst other radio emissions (including a solar type III around 0900 UT) using the Waters, Jackman, et al. (2021) empirical selection technique. By exploiting the fact that the AKR emission is distinct in frequency-time space from other sparse emission, the number of filled frequency bins has been used to select the start and end time of the burst. Similarly, the density of filled frequency bins is used to select lower and upper frequency limits at each time interval during the burst. This combination of techniques has significantly cleaned up the data presented in panel 2(a), to reveal the AKR emission presented in panel 2(e).

Resulting from this burst algorithm, there were sometimes short small repeated events that occurred in rapid succession, which can be considered as short patches of emission relating to a single coherent event. Additionally, some burst start or end times were placed in such a way as to remove a small portion of the burst, particularly for weak events. An example of this is presented in Figure 4, where panel 4(a) shows L2 Wind/WAVES data, panel 4(b) shows W21-selected data, panel 4(c) shows the number of filled frequency bins as a function of time, and 4(d) shows the burst-selected data from 24 April 2002. In this example, the tail end of the burst was removed as there was a temporary narrowing of the emission in frequency space which lasted for two time intervals.

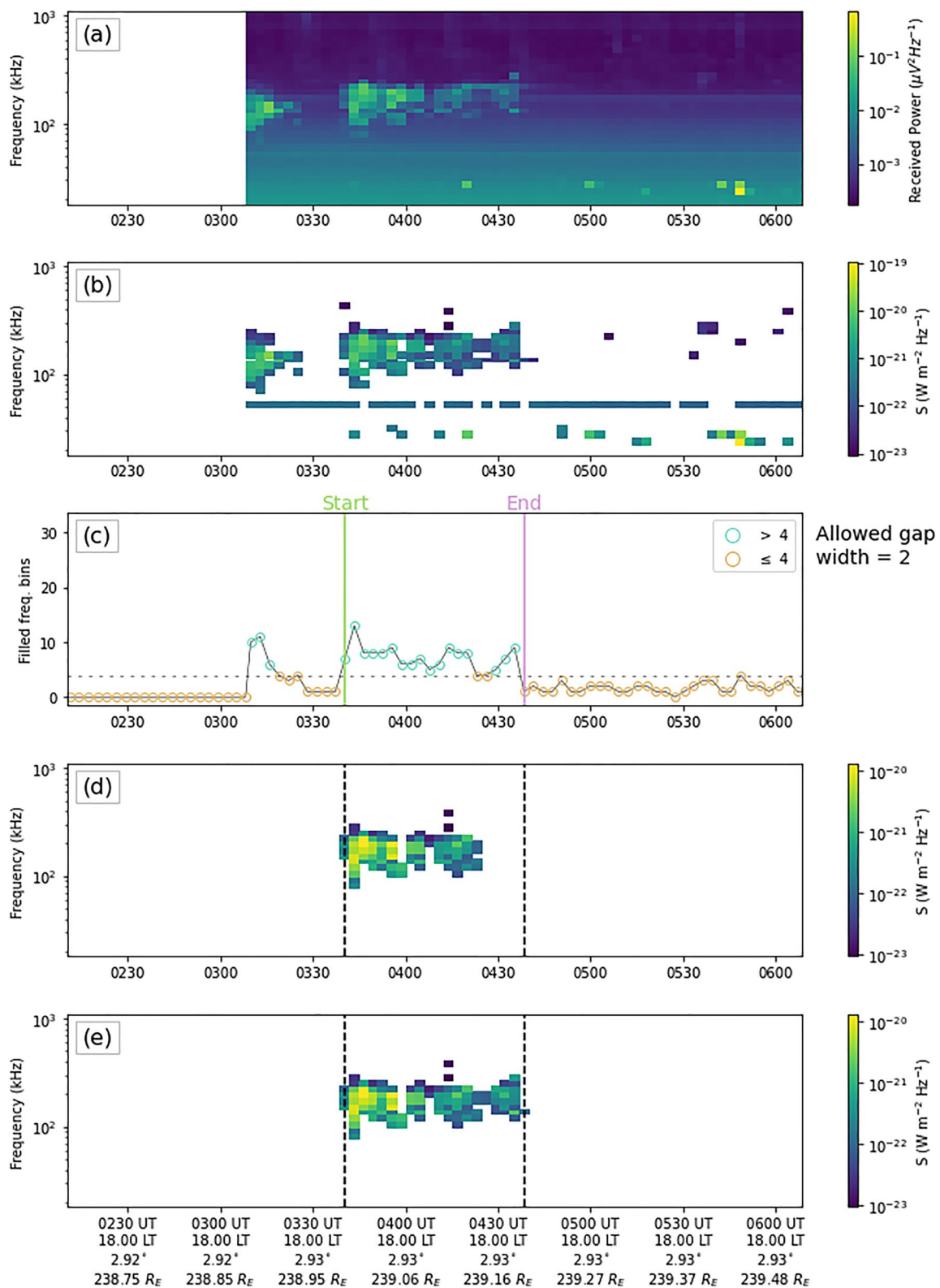


Figure 4. Frequency-time-intensity spectrogram of (a) L2 Wind/WAVES data, (b) W21-selected AKR data, (d) burst selected data before the addition of smaller bursts, (e) burst selected data after the addition of small bursts from 24 April 2002. Panel (c) shows the number of filled frequency bins as a function of time in W21-selected data shown in panel (b); empirical threshold of four bins is indicated and times meeting the condition are colored turquoise, otherwise orange. All intensities according to individual color bars. Tick labels on the x axis indicate universal time on panels (a)–(d), and universal time and spacecraft position in terms of local time, latitude, and radial distance in panel (e).

To account for this, and ensure that weaker or shorter events weren't unnecessarily removed from the event list, the algorithm was run a second time, relaxing the minimum length condition to 3 time steps (≈ 9 min). Any additional short events which were associated with a larger event from the original search - within 2 time intervals (≈ 6 min) - were kept; this new start and end time and associated frequency limits are the final burst definition. These smaller bursts were combined with their parent event, as can be seen in the final burst-selected data in Figure 4e. In this example, the tail end of the burst has been reattached to its parent event. This recombination procedure is applied to about 5% of detected events.

Finally, the power within the main AKR band is considered. The integrated power between 100 and 400 kHz is calculated during burst windows. Any events with zero integrated power in the main AKR band are removed from the event list. Events of this type are detected as there can be coherent clusters of emission at low frequencies, which are indistinguishable from AKR emission clusters until the frequency range of AKR is taken into account. Any event with no power in the 100–400 kHz range is not thought to be primarily driven by the electron cyclotron maser instability, and so is not relevant to the AKR burst event list; about 5% of events are excluded based on this criterion

For simplicity, the steps taken to create the burst event list are summarized here:

1. L2 Wind/WAVES data is processed using Waters, Jackman, et al. (2021) selection technique: an empirical threshold is applied to the standard deviation of multiple samplings of each frequency-time bin.
2. Detect burst start and end times: identify where the number of filled frequency bins meets an empirical threshold, taking into account allowed outages.
3. Select lower and upper frequency limits during burst window: find frequency limits between which a threshold on packing density is met.
4. Search for short events and combine with associated parent event: repeat burst search algorithm with relaxed minimum length condition, and keep only short events which are associated with a longer event.
5. Remove events with no power at AKR frequencies: any distinct clusters of emission at low frequencies with no component in the 100–400 kHz range are removed from the list.

Since this novel burst detection technique is automated, it is repeatable and doesn't suffer from any subjectivity issues relating to manual selection of data by a user. Additionally, it is considerably faster to select burst events from many years of data. The resulting burst-selected data, an example of which is presented in Figure 2e, shows an AKR event with a defined start and end time, as well as lower and upper frequency limits, picked out from amongst a complex mixture of signals detected by the instrument in Figure 2a. A list of these detected AKR events is provided for the community by Fogg et al. (2021, <https://doi.org/10.25935/hfjx-xx26>), and can be used in studies of terrestrial solar wind - magnetosphere - ionosphere coupling.

5. Detected AKR Burst Events

The burst search algorithm was run over all available W21-selected AKR data from 2000 to 2004 inclusive, and 5080 bursts were detected. In this section, the observing location and average characteristics of the bursts will be examined, before they are compared with solar wind data. First, the observing locations in the magnetosphere are examined, taking into account that Wind samples the near-Earth environment unevenly, as displayed in Figure 1 and discussed previously.

Figure 5 shows the distribution in LT vs radial distance grids relating to Wind's location and that of the detected events. It is important to note that the spacecraft's location is not the same as the source location. As discussed in Section 1, AKR propagates in a hollow cone at angles near perpendicular to the source region (Wu, 1985; Wu & Lee, 1979), so AKR is frequently viewed at a different LT to the LT of the source itself, also depending on the radial distance of the spacecraft. Tracing the detected AKR signal from the observation point to the source region is non-trivial, and in particular requires knowledge of the polarisation of the signal (in order to unpack the source hemisphere) which is not recorded in the Wind/WAVES data. As a consequence, the viewing positions of AKR in terms of spacecraft location (rather than the position of the source itself) are discussed from here on.

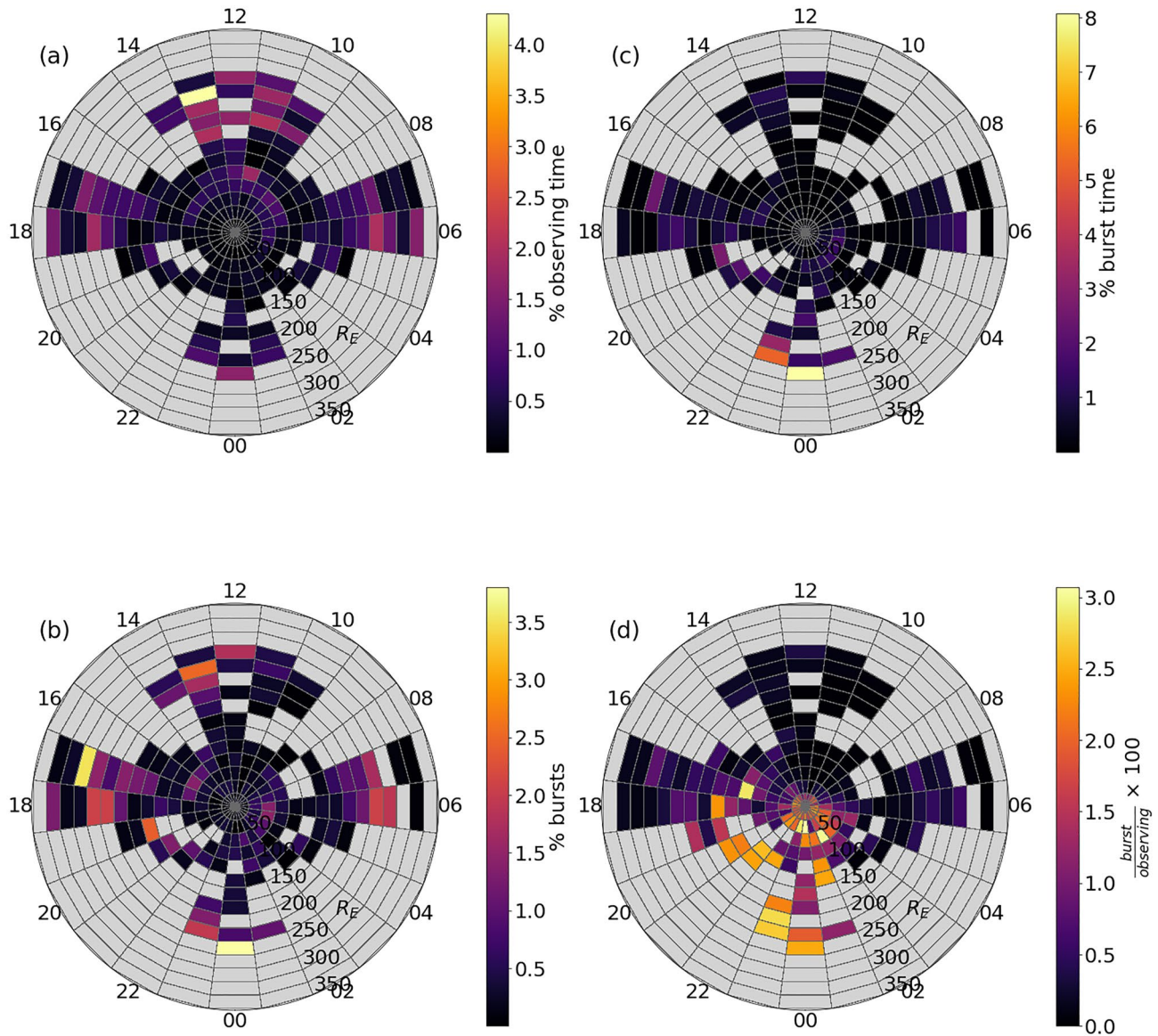


Figure 5. Spacecraft LT vs radial distance grids, with bin color indicating its share (during 2000–2004 inclusive) of (a) percentage of Wind observation time (b) percentage of detected burst events (c) percentage of burst time (intervals during selected burst windows) (d) fraction of burst time divided by fraction of observation time as percentage. Gray cells indicate zero values, color scale is unique to each panel. Noon is at the top, dawn on the right, radial distance from the Earth radii (R_E) increases with increasing radius.

First, Figure 5a shows Wind’s uneven sampling of the near-Earth environment, indicating some good viewing at near midnight, dawn, noon and dusk at a variety of radial distances. Wind spends most time in a bin close to noon, at the L1 point. The percentage of detected events observed in each of the LT x radial distance bins is presented in Figure 5b. Bursts are observed throughout the region explored by Wind, although some bins with little observing time in Figure 5a show no detected bursts.

Combining all integration intervals from all selected burst windows, the percentage of ‘burst time’ in each LT x radial distance sector is presented in Figure 5c. Although burst time is spent across a range of LT and radial distance values, the midnight sector between 200 and 300 R_E contains the largest share of burst observing time. However, since the bins are unevenly sampled by Wind, the amount of burst time has been normalised by the observing time and presented in Figure 5d. Despite the uneven sampling, a clear preference for the evening - midnight sector is observed, across a variety of radial distances. This agrees with previous work which shows

that although AKR can be observed at any LT (Zhao et al., 2019), the majority of observations are in the evening - midnight sector.

A strong LT dependence of observed AKR intensity was demonstrated in Section 3. In order to take this into account, the distributions of different characteristics (duration, intensity, frequency) for different LT sectors are presented in Figure 6. Considered are observations across all LTs (black curve) and for different LT sectors: midnight (21-3 LT, gold), dawn (3-9 LT, purple), noon (9-15 LT, green), and dusk (15-21 LT, blue).

Next, the distributions of temporal burst characteristics will be discussed. Throughout this study, temporal parameters are measured in units of 'integration intervals', essentially the time resolution of the frequency-intensity spectrogram, such as those presented in Figure 2. Wind/WAVES integration intervals are around three minutes and three seconds, with a variable number of decimal seconds. For that reason, over the statistical analyses in this study integration intervals are used as an even measurement of temporal characteristics. These intervals can be used to make an estimation of the time in minutes: three times the number of integration intervals is approximately the number of minutes; this is plotted on the top axis of panels (a-c) in Figure 6 for ease of interpretation.

Broadly, the distributions of burst duration (Figure 6a) are similar across different LTs. The midnight (gold) curve peaks lower than the curve for all LTs (black) and the noon (green) curve. Across the different curves, the median duration is between 10 and 13 integration intervals (roughly 30 and 39 min) for all curves except the midnight sector, which is notably 21 integration intervals (roughly 63 min). Multiplying by three gives a rough indication of the minutes this equates to: about an hour for bursts observed at midnight, and around half an hour elsewhere. A combination of factors will be in play here; firstly, due to the anisotropic beaming of AKR, it is more likely to be viewed from midnight local times, meaning that other LTs may see a shorter portion of a longer event as the emission cone changes location. Additionally, for AKR produced at different LT, the driving mechanisms may differ. Transient enhancements of dayside field aligned currents relating to upwelling and downwelling electrons, which could generate similar emission under the right circumstances, may produce shorter bursts of emission than nightside drivers such as substorms. A median burst length of about an hour for nightside bursts is in keeping with substorm timescales of the same order (Forsyth et al., 2015, and references therein).

Similarly, the distributions of repeating interval (time since the beginning of previous burst, Figure 6b) and separation interval (time since the end of previous burst, Figure 6c) are similar across different local times, with slight differences in the height of the peaks for midnight and noon. The median values presented in Table 1 indicate longer waiting times between bursts as the observer moves toward noon. This agrees with the notion that AKR is observed more regularly in the midnight than noon sectors; a similar value is found for dawn and dusk in both cases. For all LTs, the median repeating interval is 46 integration intervals (roughly 2 hr and 18 min), and median separation between bursts of 15 integration intervals (roughly 45 min). For observations from the midnight sector, a median repeat time of 38 integration intervals is recorded, equating to just under 2 hr, comparable with substorm repeating timescales of approximately, 1-4 hr (e.g., Freeman & Morley, 2004; Forsyth et al., 2015; Huang et al., 2004; Lee et al., 2006).

Figure 6 panels (d-f) show distributions of starting, median and maximum fractional intensity above the LT background described in Section 3. This fractional intensity is the observed integrated intensity divided by the LT-intensity variation (black curve Figure 3b), and so values above one are brighter than the usual observed intensity, and values less than one are less bright than usual. Across the different LT regions, the curves are broadly similar, although a higher peak is seen for midnight (gold) for Figure 6 panels (d-f). Median values for these curves presented in Table 1 show values that are lower for the starting intensity than the median, suggesting that the AKR emission becomes brighter as the burst continues. Across all LT regions, the median intensity is about 1.5 times the LT background, showing that the detected bursts are brighter than the average background emission. This effect is lowest at midnight LTs, where the median intensity is lower than the LT background, and the maximum intensity is the lowest of all LT regions. The median and maximum fractional intensity is highest above the LT background at noon LTs, perhaps suggesting that there is greater variability in AKR intensity at noon as AKR is least frequently observed there, compared with midnight where it is most often observed.

Finally, distributions of burst characteristics relating to observed frequencies are presented in Figure 6 panels (g-i). Although dawn (purple) and dusk (blue) curves mostly follow the trends for all LTs, noon (green) and midnight (gold) show some differences. For bursts observed at midnight, the distribution of maximum observed

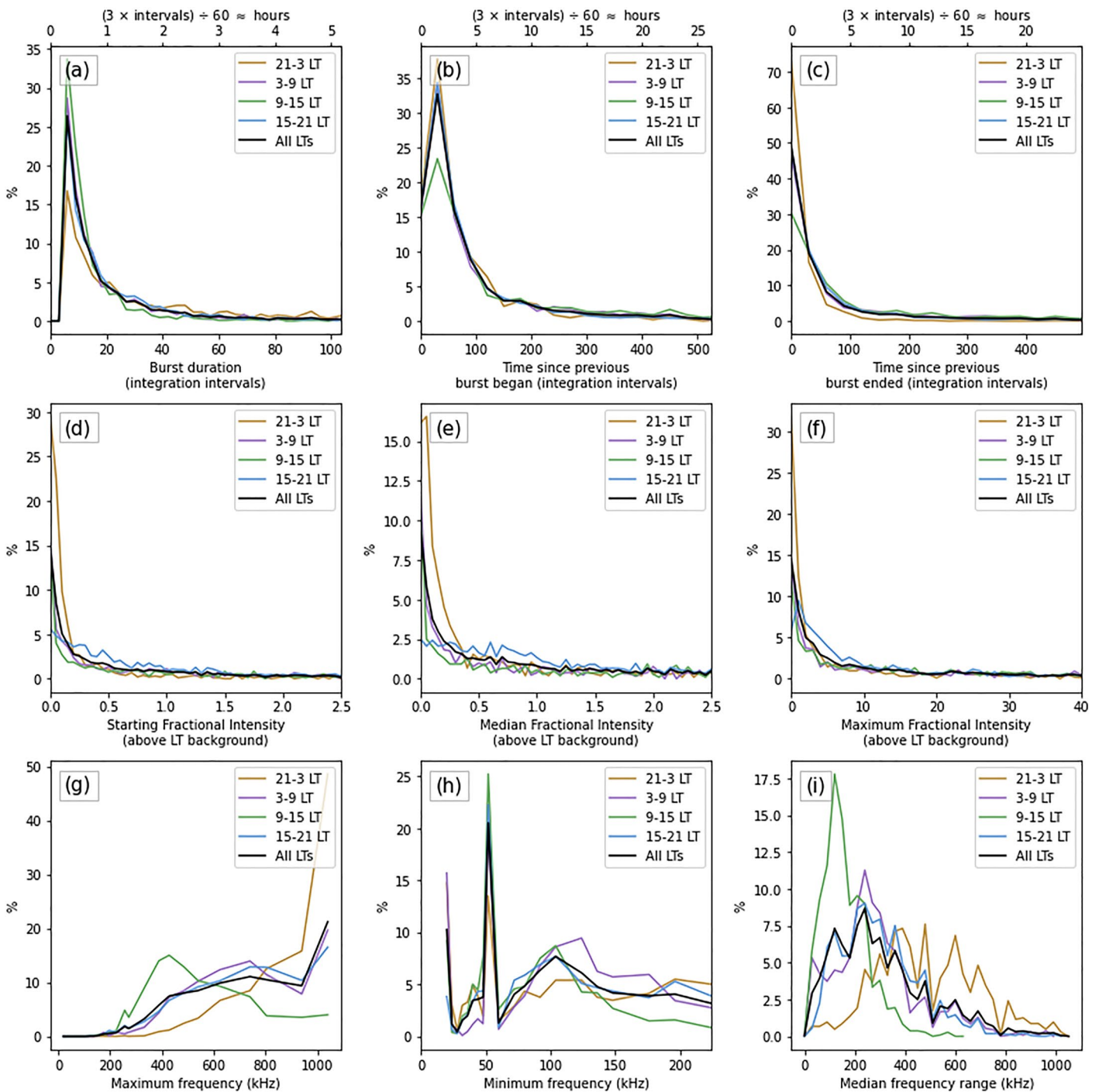


Figure 6. For single value burst characteristics calculated over the each burst window, distributions of (a) burst duration (b) time since the start of previous burst (c) time since the end of previous burst (d) starting intensity (e) median intensity (f) maximum intensity (g) maximum frequency (h) minimum frequency (i) median frequency range. Temporal characteristics in (a)–(c) are in integration intervals, with approximate hours labeled on the top axis. Intensity values are fraction above LT background described in Section 3. For frequency limits in (g) and (h) discrete histogram bins are based on the standard sampling frequencies, otherwise bins are equally spaced with widths: (a) 3 integration intervals (b) 30 integration intervals (c) 30 integration intervals (d) 0.05 (e) 0.05 (f) 1.0 (i) 30 kHz. The x axis is limited to show the majority of the data for all panels except (g) and (i).

Table 1
Median Values of the Distributions Presented in Figure 6, in Same Units

LT sector	Temporal			Intensity			Frequency		
	(integration intervals)			(fraction of LT background)			(kHz)		
	(a) duration	(b) repeat	(c) Separation	(d) starting	(e) median	(f) max	(g) Max	(h) min	(i) range
Midnight	21.0	38.0	6.0	0.068	0.201	2.619	940.0	60.0	472.0
21-3 LT									
Dawn	11.0	45.0	19.0	1.152	2.488	27.276	740.0	92.0	260.0
3-9 LT									
Noon	10.0	64.0	45.0	2.525	4.662	29.506	484.0	52.0	150.0
9-15 LT									
Dusk	13.0	43.0	16.0	0.800	1.619	11.589	740.0	80.0	280.0
15-21 LT									
All LT	12.0	46.0	15.0	0.696	1.549	14.509	740.0	72.0	268.0

Note. Intensity measurements are fractions above LT background, to three decimal places. Columns are labeled with the panel labels from Figure 6, indicating the parameter in question.

frequencies (Figure 6g) has a higher peak at high frequencies, with a median of 940 kHz, elevated above the value for all LTs (740 kHz). For bursts observed at noon, the distribution of maximum observed frequencies peaks at lower frequencies than for bursts at all LTs. The frequency range of each burst varies with time, and is the difference between the upper and lower frequency limits at a given time - the distribution of the median values of frequency range within each burst window are presented in Figure 6i. For bursts observed in the noon (green) sector, the distribution peaks at much lower frequencies than other LTs, and doesn't extend far beyond 600 kHz. Conversely, for bursts observed in the midnight sector, the distribution is shifted to higher frequency ranges, and flattened when compared with noon events. This could be interpreted as an indicator of more low-frequency extension (LFE) events observed in the midnight sector, but certainly shows a difference in the morphology of detected bursts in frequency space when compared with all other LTs.

6. Solar Wind and Geomagnetic Indices During Burst Windows

The automated detection technique presented above allows examination of AKR events on statistical timescales. Here, the statistical characteristics of solar wind parameters and geomagnetic indices during burst windows will be compared with the average characteristics during the entire statistical window (2000–2004). For the upstream parameters including IMF components and solar wind characteristics which are propagated to the bow shock in the OMNI catalog, the value of a parameter at the burst onset is not necessarily the same as any change driving the dynamics of the source region. This is especially true for AKR source regions in the magnetotail, where the propagation of the effects of dayside onset of magnetic reconnection into the tail, for example, can take of the order of hours (e.g., Milan, 2015). However, to analyze the statistical properties of the solar wind and IMF which trigger the burst, a 'driving' interval before the burst onset would need to be chosen. Since this is still an open question, the upstream characteristics during the burst window are considered, as they are likely to be similar to those that came before (except in circumstances of rapid changes e.g., infrequent rapid magnetopause compressions).

The distributions during the five year interval (black), during burst windows (purple), and during bursts within top 10% median intensity (orange), for various IMF, solar wind, and geomagnetic indices are presented together in Figure 7. First, the distribution of the IMF clock angle will be considered, as presented in Figure 7a. Notably, the distribution for all curves shows more intervals with an IMF B_y component than without; this is related to the average angle the Parker spiral makes with the Sun-Earth line at 1 AU, of about 45° (e.g., Thomas & Smith, 1980). A similarly shaped distribution of clock angle values with more observations with a B_y component than without was observed at Mercury by James et al. (2017) in MESSENGER data. Comparing the curves for the entire interval and for burst windows only, there is a shift toward $B_z < 0$, $B_y < 0$ in burst windows; for events

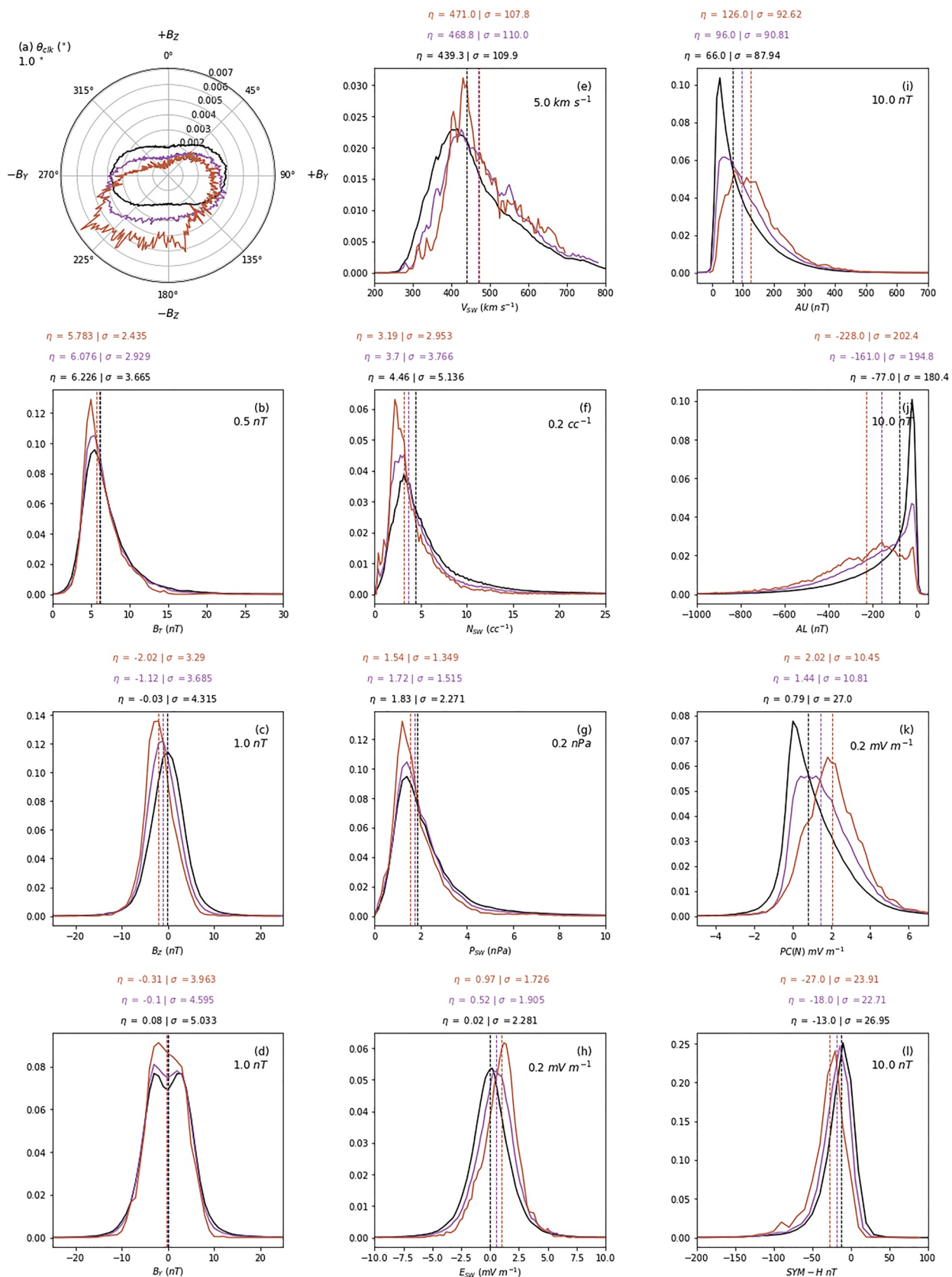


Figure 7.

with the highest intensity, the distribution moves even further toward $B_z < 0$, $B_y < 0$. It is well known that $B_z < 0$ allows for dayside reconnection at the subsolar point, and that a great deal of energy can be communicated into the magnetosphere in such situations. However, it has also been shown that a component of IMF B_y can also enable dayside reconnection (e.g., Grocott et al., 2003; Grocott et al., 2004, 2008), albeit changing the location of the reconnection sites (Trenchi et al., 2008), again allowing energy transfer between the solar wind and the terrestrial magnetosphere. Gallagher and D'Angelo (1981) showed that the existence of a B_y component in the IMF resulted in enhanced AKR intensity, and as in this study, Desch et al. (1996) showed that AKR events preferentially occur under $B_y < 0$ conditions. Indeed, for events with the highest intensity, an even stronger preference for $B_z < 0$, $B_y < 0$ is observed in this study.

The distributions of IMF magnetic field magnitude (B_T , Figure 7b) for the datasets are broadly similar, although the curves for burst intervals only have slightly smaller standard deviations. For IMF B_z (Figure 7c), the median value is shifted from around zero for the entire five year data set, to -1.12 nT for during burst windows, and further to -2.02 nT for the most intense events. This suggests that IMF $B_z < 0$ is likely to be observed around burst onset, allowing greater energy transfer between the solar wind and magnetosphere, and that stronger IMF $B_z < 0$ results in the most intense AKR emissions. The curves for IMF B_y , presented in Figure 7d show similar twin peaked distributions for both the black and purple curves (with similar medians around zero), and a broad peak for the most intense events (orange), with a slightly more negative median; the twin peaked shapes relate to the flat shape of the clock angle plot explained above. This suggests that the most intense events are more often linked to IMF $B_y < 0$ conditions. For both B_z and B_y , the distributions during burst windows show a slightly smaller standard deviation, meaning there is less variability, and so more specific conditions are observed.

Next, the solar wind parameters presented in the middle column of Figure 7 will be discussed. The solar wind flow velocity, V_{sw} shows a similar shape distribution for all three datasets with similar standard deviations in Figure 7e, shifted to higher values for burst windows, with a median that is 29.5 km s^{-1} higher (around 7%, the value is similar for the most intense events). This confirms results by Desch et al. (1996) who showed more radio events occurring at times of higher solar wind speed. For solar wind proton density, presented in Figure 7f, the distribution for all burst windows is sharper with a standard deviation about 27% smaller, and shifted to lower values with a median about 17% smaller. For the most intense events, the median is 28% smaller than for all intervals, with a standard deviation 43% smaller - suggesting that lower solar wind density precedes the most intense events.

The curves for solar wind dynamic pressure, $\approx N_{sw} V_{sw}^2$, are presented in Figure 7g, and show a similar distribution for both datasets, with a similar median. Given the slightly higher solar wind velocity (which is squared in the calculation of pressure), and markedly lower proton density during burst windows, a similar median for the datasets is consistent. The standard deviation of the curve for P_{sw} is about a third smaller for burst windows (about 41% for the most intense events), suggesting less spread of the data, and perhaps less extreme values. The medians of the distributions are 6% smaller for burst windows (16% for the most intense events). Lastly, the solar wind electric field, $\approx -V_{sw} B_z$ shows a shift from a median of about zero for the entire five year data set to a small magnitude but positive median of 0.52 mV m^{-1} for all burst windows, and a 16% smaller standard deviation. For the most intense events, the distribution moves further toward positive electric field, with a median of 0.97 mV m^{-1} , and a standard deviation 24% smaller than for all intervals.

Finally, the distributions of geomagnetic indices (described previously in Section 2) for the entire five year data set and during burst windows will be examined. In this instance, the indices are all derived from ground based magnetometer stations, so although there may be some time difference between the index enhancement and that of the AKR, it will be much smaller than the difference between the bow shock onset of a solar wind change and any related AKR enhancement. Broadly speaking, the geomagnetic indices will be enhanced roughly simultane-

Figure 7. Distribution of IMF, solar wind, and geomagnetic indices during the entire statistical interval (black), during burst windows only (purple), and during the burst windows within the top 10% of median intensity (orange, as presented in Figure 6c). Panels show (a) IMF clock angle: $\theta_{clk} = \tan^{-1} \left(\frac{B_y}{B_z} \right)$ (b) IMF magnetic field magnitude: $B_T = \sqrt{B_x^2 + B_y^2 + B_z^2}$ (c) IMF B_z (d) IMF B_y (e) solar wind velocity V_{sw} (f) solar wind proton density N_{sw} (g) solar wind dynamic pressure: $P_{sw} \approx N_{sw} V_{sw}^2$ (h) solar wind electric field $E_{sw} \approx -V_{sw} B_z$ (i) AU (j) AL (k) PC(N) (l) SYM-H. Histogram bins are of equal width indicated under the panel label letter. Median (η) and standard deviation (σ) are written above each panel, with a dashed line indicating the position of the median. There is no median or standard deviation for the clock angle as it is a periodic variable. Limits of x axis have been manually chosen to show clearly more than 90% of the data, and as such some of the distributions extend further beyond this at low occurrence values.

ously to any corresponding AKR enhancement. For example, the auroral electrojet index (AE) has been shown to correlate well with AKR enhancements relating to substorms (e.g., Dunckel et al., 1970; Gurnett, 1974; Voots et al., 1977). Here, the upper and lower envelopes of AE (AU and AL respectively) are considered, as they will show positive and negative enhancements in the auroral zone (notably AL is a well known substorm indicator).

For AU, the distribution during burst windows exhibits a median about 31% higher, and a standard deviation about 3% higher than for all intervals, as presented in Figure 7i. For the most intense events, the median of the distribution is 48% higher than for all intervals, with a standard deviation 5% higher. Although the distributions peak at similar values, the peak is smaller and the spread is wider for burst windows, and more so for the most intense events. For AL, presented in Figure 7j, the median for burst windows is over twice as negative when compared with all intervals, and the standard deviation is about 7% higher. For the most intense events, the median is almost three times a negative when compared with all intervals, with a standard deviation about 10% higher. For both burst window curves, a shorter peak is observed, with a wider spread. Significantly higher magnitude values are observed for both AU and AL, indicating greater activity at auroral latitudes in the ionosphere during burst windows, and even further enhancements during the most intense events.

Distributions for the northern (geographic) hemisphere polar cap index PC(N) are presented in Figure 7k, showing a shift toward more positive values during burst windows. All burst windows exhibit a median over 80% larger than for all values, indicating greater geomagnetic disturbance in the polar cap, roughly meaning faster antisunwards movement of open flux, or equivalently stronger ionospheric electrodynamics. This effect is larger for the most intense events, where the median is 2.6 times larger than for all intervals. Additionally, for both sets of burst windows the standard deviation is less than half the spread for all intervals, indicating less variability in the data. The median for SYM-H (Figure 7l) during burst windows is about 38% larger than for all intervals (more than twice as negative for the most intense events), and shows a decrease in the standard deviation for both sets of burst windows, indicating less variability.

7. Conclusion

In this study, a novel technique which automates the detection of AKR bursts has been presented, and applied to five years of data from the Wind/WAVES instrument. This automated method is a powerful tool since it removes non-AKR signals such as solar type III bursts and RFI signals. Over a statistical survey of five years, about 5000 bursts were detected, and their temporal, spatial, frequency and intensity characteristics have been presented, as well as average solar wind parameters and geomagnetic indices during burst windows. Some key results from these analyses are listed below:

1. Average observed AKR intensities vary up to two orders of magnitude between different local time sectors.
2. Detected bursts were preferentially viewed in the dusk to midnight LT sector, at a range of radial distances.
3. Median AKR burst duration varied from about half an hour for all LTs, to an hour for bursts observed in the midnight sector.
4. The median repeating interval between burst onsets was roughly two hours.
5. Midnight bursts displayed a wider median frequency range than all LTs, perhaps indicating more LFEs. Conversely, bursts observed from noon showed more narrow frequency ranges than for all LTs.
6. The IMF clock angle distribution was shifted toward $B_z < 0$, $B_y < 0$ during burst windows.
7. During burst windows, the observed solar wind velocity was about 30 km s^{-1} faster than for the entire statistical interval.
8. Higher geomagnetic activity was seen in the AU, AL, PC(N) and SYM-H indices during burst windows.
9. For the most intense AKR bursts, further enhancements were observed in B_z , B_y , V_{SW} , and geomagnetic indices AU, AL, PC(N), and SYM-H.

The development of an automated AKR burst detection algorithm as presented here unlocks the potential of AKR as a quasi-continuous remote monitor of terrestrial solar wind - magnetosphere - ionosphere coupling. The use of an automated technique based on empirical criteria removes the subjectivity and time-consuming nature of selecting them by eye. As well as the potential for this technique to be applied to the entire Wind/WAVES data set, which would enable statistical analysis of solar wind - magnetosphere coupling effects on AKR, the technique could also be adapted for other AKR observing spacecraft. Indeed, there is also the potential for this technique

to be adapted to automatically select distinct sources of emission from radio spectra at other planets, for example Saturn Kilometric Radiation, which is analogous to AKR.

A catalog of detected events has been provided for community use, and can be downloaded here: Fogg et al. (2021, <https://doi.org/10.25935/hfjx-xx26>). There are many potential future avenues for comparison of these detected AKR bursts with other metrics of geomagnetic activity, all in parallel with careful consideration of the viewing constraints associated with the anisotropically beamed emission from LT-restricted sources.

Data Availability Statement

Wind/WAVES data that has been empirically selected for AKR emissions using the technique by Waters, Jackman, et al. (2021), and a subset is available online (Waters, Cecconi, et al., 2021, <https://doi.org/10.25935/wxv0-vr90>). The AKR burst list developed in this study is available online: Fogg et al. (2021, <https://doi.org/10.25935/hfjx-xx26>). OMNI data including AU, AL, PC(N), and SYM-H indices were obtained via OMNIWeb (<https://omniweb.gsfc.nasa.gov/hw.html>).

References

- Benson, R. F., & Calvert, W. (1979). ISIS 1 observations at the source of auroral kilometric radiation. *Geophysical Research Letters*, 6(6). <https://doi.org/10.1029/GL006i006p00479>
- Benson, R. F., Calvert, W., & Klumpar, D. M. (1980). Simultaneous wave and particle observations in the auroral kilometric radiation source region. *Geophysical Research Letters*, 7(11), 959–962. <https://doi.org/10.1029/GL007i011p00959>
- Bougeret, J. L., Kaiser, M. L., Kellogg, P. J., Manning, R., Goetz, K., Monson, S. J., et al. (1995). WAVES: The radio and plasma wave investigation on the Wind spacecraft. *Space Science Reviews*, 71, 231–263. <https://doi.org/10.1007/BF00751331>
- Calvert, W. (1981a). The AKR emission cone at low frequencies. *Geophysical Research Letters*, 8(11), 1159–1162. <https://doi.org/10.1029/GL008i011p01159>
- Calvert, W. (1981b). The auroral plasma cavity. *Geophysical Research Letters*, 8(8), 919–921. <https://doi.org/10.1029/GL008i008p00919>
- Davis, T. N., & Sugiura, M. (1966). Auroral electrojet activity index AE and its universal time variations. *Journal of Geophysical Research*, 71(3), 785–801. <https://doi.org/10.1029/JZ071i003p00785>
- Desch, M. D. (1982). Evidence for solar wind control of Saturn radio emission. *Journal of Geophysical Research*, 87(A6), 4549–4554. <https://doi.org/10.1029/JA087iA06p04549>
- Desch, M. D., Kaiser, M. L., & Farrell, W. M. (1996). Control of terrestrial low frequency bursts by solar wind speed. *Geophysical Research Letters*, 23(10), 1251–1254. <https://doi.org/10.1029/96GL01352>
- Desch, M. D., & Rucker, H. O. (1983). The relationship between Saturn kilometric radiation and the solar wind. *Journal of Geophysical Research*, 88(A11), 8999–9006. <https://doi.org/10.1029/JA088iA11p08999>
- Dunckel, N., Ficklin, B., Rorden, L., & Helliwell, R. A. (1970). Low-frequency noise observed in the distant magnetosphere with OGO 1. *Journal of Geophysical Research*, 75(10). <https://doi.org/10.1029/JA075i010p01854>
- Dungey, J. W. (1961). Interplanetary magnetic field and the auroral zones. *Physical Review Letters*, 6(2), 47. <https://doi.org/10.1103/PhysRevLett.6.47>
- Ergun, R. E., Carlson, C. W., McFadden, J. P., Mozer, F. S., Delory, G. T., Peria, W., et al. (1998). FAST satellite wave observations in the AKR source region. *Geophysical Research Letters*, 25, 2061–2064. <https://doi.org/10.1029/98GL00570>
- Fogg, A. R., Jackman, C., Waters, J. E., Bonnin, X., Lamy, L., Cecconi, B., et al. (2021). *Bursts of auroral kilometric radiation individually selected from wind/waves data*. version 1.0.
- Forsyth, C., Rae, I. J., Coxon, J. C., Freeman, M. P., Jackman, C. M., Gjerloev, J., & Fazakerley, A. N. (2015). A new technique for determining Substorm Onsets and Phases from Indices of the Electrojet (SOPHIE). *Journal of Geophysical Research: Space Physics*, 120, 10592–10606. <https://doi.org/10.1002/2015JA021343>
- Freeman, M. P., & Morley, S. K. (2004). A minimal substorm model that explains the observed statistical distribution of times between substorms. *Geophysical Research Letters*, 31. <https://doi.org/10.1029/2004GL019989>
- Gallagher, D. L., & D'Angelo, N. (1981). Correlations between solar wind parameters and auroral kilometric radiation intensity. *Geophysical Research Letters*, 8(10), 1087–1089. <https://doi.org/10.1029/GL008i010p01087>
- Gallagher, D. L., & Gurnett, D. A. (1979). Auroral kilometric radiation: Time-averaged source location. *Journal of Geophysical Research*, 84(A11). <https://doi.org/10.1029/JA084iA11p06501>
- Green, J. L., Boardson, S., Garcia, L., Fung, S. F., & Reinisch, B. W. (2003). Seasonal and solar cycle dynamics of the auroral kilometric radiation source region. *Journal of Geophysical Research*, 109, A05223. <https://doi.org/10.1029/2003JA010311>
- Green, J. L., & Gallagher, D. L. (1985). The detailed intensity distribution of the AKR emission cone. *Journal of Geophysical Research*, 90(A10), 9641–9649. <https://doi.org/10.1029/JA090iA10p09641>
- Green, J. L., & Gurnett, D. A. (1979). A correlation between auroral kilometric radiation and inverted V electron precipitation. *Journal of Geophysical Research*, 84(A9). <https://doi.org/10.1029/JA084iA09p05216>
- Green, J. L., Gurnett, D. A., & Shawhan, S. D. (1977). The angular distribution of auroral kilometric radiation. *Journal of Geophysical Research*, 82(13). <https://doi.org/10.1029/JA082i013p01825>
- Grocott, A., Badman, S. V., Cowley, S. W. H., Yeoman, T. K., & Cripps, P. J. (2004). The influence of IMF By on the nature of the nightside high-latitude ionospheric flow during intervals of positive IMF Bz. *Annales Geophysicae*, 22(5), 1755–1764. <https://doi.org/10.5194/angeo-22-1755-2004>
- Grocott, A., Cowley, S. W. H., & Sigwarth, J. B. (2003). Ionospheric flow during extended intervals of northward but B_y -dominated IMF. *Annales Geophysicae*, 21(2), 509–538. <https://doi.org/10.5194/angeo-21-509-2003>
- Grocott, A., Milan, S. E., & Yeoman, T. K. (2008). Interplanetary magnetic field control of fast azimuthal flows in the nightside high-latitude ionosphere. *Geophysical Research Letters*, 35(8). <https://doi.org/10.1029/2008GL033545>

Acknowledgments

A.R.F., C.M.J. and C.K.L.'s work is supported by the Science Foundation Ireland Grant 18/FRL/6199. J.E.W.'s work was supported by the EPSRC Centre for Doctoral Training in Next Generation Computational Modelling Grant No. EP/L015382/1. The authors acknowledge CNES (Centre National d'Etudes Spatiales), CNRS (Centre National de la Recherche Scientifique) / INSU (Institut national des sciences de l'Univers) programs of planetology and heliophysics, and Observatoire de Paris for support to the Wind/WAVES team and the CDPP (Centre de Données de la Physique des Plasmas) for the provision of the Wind/WAVES RAD1 L2 data. The authors gratefully acknowledge use of NASA/GSFC's Space Physics Data Facility's OMNIWeb service, and OMNI data. The AU, AL and SYM-H indices used in this paper/presentation were provided by the WDC for Geomagnetism, Kyoto (<http://wdc.kugi.kyoto-u.ac.jp/wdc/Sec3.html>) via OMNIWeb. PC(N) index was provided by World Data Center for Geomagnetism, Copenhagen via OMNIWeb.

- Gurnett, D. A. (1974). The earth as a radio source: Terrestrial kilometric radiation. *Journal of Geophysical Research*, 79(28). <https://doi.org/10.1029/JA079i028p04227>
- Hashimoto, K., Matsumoto, H., Murata, T., Kaiser, M. L., & Bougeret, J.-L. (1998). Comparison of AKR simultaneously observed by the GEOTAIL and WIND spacecraft. *Geophysical Research Letters*, 25(6), 853–856. <https://doi.org/10.1029/98GL00385>
- Hilgers, A. (1992). The auroral radiating plasma cavities. *Geophysical Research Letters*, 19(3), 237–240. <https://doi.org/10.1029/91GL02938>
- Huang, C.-S., Le, G., & Reeves, G. D. (2004). Periodic magnetospheric substorms during fluctuating interplanetary magnetic field B_z . *Geophysical Research Letters*, 31, L14801. <https://doi.org/10.1029/2004GL020180>
- Huff, R. L., Calvert, W., Craven, J. D., Frank, L. A., & Gurnett, D. A. (1988). Mapping of auroral kilometric radiation sources to the aurora. *Journal of Geophysical Research*, 93(A10), 11445–11454. <https://doi.org/10.1029/JA093iA10p11445>
- Iyemori, T. (1990). Storm-time magnetospheric currents inferred from mid-latitude geomagnetic field variations. *Journal of Geomagnetism and Geoelectricity*, 42(11), 1249–1265. <https://doi.org/10.5636/jgg.42.1249>
- Jackman, C. M., Arridge, C. S., Slavin, J. A., Milan, S. E., Lamy, L., Dougherty, M. K., & Coates, A. J. (2010). In situ observations of the effect of a solar wind compression on Saturn's magnetotail. *Journal of Geophysical Research*, 115, A10240. <https://doi.org/10.1029/2010JA015312>
- James, M. K., Imber, S. M., Bunce, E. J., Yeoman, T. K., Lockwood, M., Owens, M. J., & Slavin, J. A. (2017). Interplanetary magnetic field properties and variability near Mercury's orbit. *Journal of Geophysical Research: Space Physics*, 122, 7907–7924. <https://doi.org/10.1002/2017JA024435>
- Janhunen, P., Olsson, A., & Laakso, H. (2002). Altitude dependence of plasma density in the auroral zone. *Annales Geophysicae*, 20, 1743–1750. <https://doi.org/10.5194/angeo-20-1743-2002>
- Johnson, M. T., Wygant, J. R., Cattell, C., Mozer, F. S., Temerin, M., & Scudder, J. (2001). Observations of the seasonal dependence of the thermal plasma density in the Southern Hemisphere auroral zone and polar cap at 1 R_E . *Journal of Geophysical Research*, 106(A9), 19023–19033. <https://doi.org/10.1029/2000JA900147>
- Kaiser, M. L., Alexander, J. K., Riddle, A. C., Pearce, J. B., & Warwick, J. W. (1978). Direct measurements by Voyagers 1 and 2 of the polarization of terrestrial kilometric radiation. *Geophysical Research Letters*, 5(10). <https://doi.org/10.1029/GL005i010p00857>
- Kasaba, Y., Matsumoto, H., & Hashimoto, K. (1997). The angular distribution of auroral kilometric radiation observed by the GEOTAIL spacecraft. *Geophysical Research Letters*, 24(20), 2483–2486. <https://doi.org/10.1029/97GL02599>
- King, J. H., & Papitashvili, N. E. (2005). Solar wind spatial scales in and comparisons of hourly Wind and ACE plasma and magnetic field data. *Journal of Geophysical Research*, 110(A2). <https://doi.org/10.1029/2004JA010649>
- Kurth, W. S., Murata, T., Lu, G., Gurnett, D. A., & Matsumoto, H. (1998). Auroral kilometric radiation and the auroral electrojet index for the January 1997 magnetic cloud event. *Geophysical Research Letters*, 25, 3027–3030. <https://doi.org/10.1029/98GL00404>
- Lamy, L., Zarka, P., Cecconi, B., & Prangé, R. (2010). Auroral kilometric radiation diurnal, semidiurnal, and shorter term modulations disentangled by Cassini. *Journal of Geophysical Research*, 115, A09221. <https://doi.org/10.1029/2010JA015434>
- Lamy, L., Zarka, P., Cecconi, B., Prangé, R., Kurth, W. S., & Gurnett, D. A. (2008). Saturn kilometric radiation: Average and statistical properties. *Journal of Geophysical Research*, 113, A07201. <https://doi.org/10.1029/2007JA012900>
- Lee, D. Y., Lyons, L. R., Kim, K. C., Baek, J. H., Kim, K. H., Kim, H. J., et al. (2006). Repetitive substorms caused by Alfvénic waves of the interplanetary magnetic field during high-speed solar wind streams. *Journal of Geophysical Research*, 111, A12214. <https://doi.org/10.1029/2006JA011685>
- Lepping, R. P., Acuña, M. H., Burlaga, L. F., Farrell, W. M., Slavin, J. A., Schatten, K. H., et al. (1995). The wind magnetic field investigation. *Space Science Reviews*, 71, 207–229. <https://doi.org/10.1007/BF00751330>
- Lin, R. P., Anderson, K. A., Ashford, S., Carlson, C., Curtis, D., Ergun, R., et al. (1995). A three-dimensional plasma and energetic particle investigation for the Wind spacecraft. *Space Science Reviews*, 71, 125–153. <https://doi.org/10.1007/BF00751328>
- Louarn, P., & Le Quéau, D. (1996). Generation of the auroral kilometric radiation in plasma cavities - II. The cyclotron maser instability in small size sources. *Planetary and Space Science*, 44(3), 211–224. [https://doi.org/10.1016/0032-0633\(95\)00122-0](https://doi.org/10.1016/0032-0633(95)00122-0)
- Milan, S. E. (2015). Sun et Lumière: Solar wind-magnetosphere coupling as deduced from ionospheric flows and polar auroras. In S. W. Cowley, D. Southwood, & S. Mitton (Eds.), *Magnetospheric Plasma Physics: The Impact of Jim Dungey's Research* (pp. 33–64). Springer. https://doi.org/10.1007/978-3-319-18359-6_2
- Morioka, A., Miyoshi, Y., Kurita, S., Kasaba, Y., Angelopoulos, V., Misawa, H., et al. (2013). Universal time control of AKR: Earth as a spin-modulated variable radio source. *Journal of Geophysical Research: Space Physics*, 118, 1123–1131. <https://doi.org/10.1002/jgra.50180>
- Morioka, A., Miyoshi, Y., Tsuchiya, F., Misawa, H., Kasaba, Y., Asozu, T., et al. (2011). On the simultaneity of substorm onset between two hemispheres. *Journal of Geophysical Research*, 116, A04211. <https://doi.org/10.1029/2010JA016174>
- Morioka, A., Miyoshi, Y., Tsuchiya, F., Misawa, H., Sakanoi, T., Yumoto, K., et al. (2007). Dual structure of auroral acceleration regions at substorm onsets as derived from auroral kilometric radiation spectra. *Journal of Geophysical Research*, 112, A06245. <https://doi.org/10.1029/2006JA012186>
- Mutel, R. L., Christopher, I. W., & Pickett, J. S. (2008). Cluster multispacecraft determination of AKR angular beaming. *Geophysical Research Letters*, 35. <https://doi.org/10.1029/2008GL033377>
- Mutel, R. L., Gurnett, D. A., & Christopher, I. W. (2004). Spatial and temporal properties of AKR burst emission derived from Cluster WBD VLBI studies. *Annales Geophysicae*, 22, 2625–2632. <https://doi.org/10.5194/angeo-22-2625-2004>
- Ogilvie, K. W., Chornay, D. J., Fritzenreiter, R. J., Hunsaker, F., Keller, J., Lobell, J., et al. (1995). SWE, a comprehensive plasma instrument for the Wind Spacecraft. *Space Science Reviews*, 71, 55–75. <https://doi.org/10.1007/BF00751326>
- Panchenko, M., Khodachenko, M. L., Kislyakov, A. G., Rucker, H. O., Hanasz, J., Kaiser, M. L., et al. (2009). Daily variations of auroral kilometric radiation observed by STEREO. *Geophysical Research Letters*, 36. <https://doi.org/10.1029/2008GL037042>
- Pritchett, P. L., Strangeway, R. J., Ergun, R. E., & Carlson, C. W. (2002). Generation and propagation of cyclotron maser emissions in the finite auroral kilometric radiation source cavity. *Journal of Geophysical Research*, 107(A12). <https://doi.org/10.1029/2002JA009403>
- Stauning, P. (2013). The Polar Cap index: A critical review of methods and a new approach. *Journal of Geophysical Research: Space Physics*, 118, 5021–5038. <https://doi.org/10.1002/jgra.50462>
- Taubenschuss, U., Rucker, H. O., Kurth, W. S., Cecconi, B., Zarka, P., Dougherty, M. K., & Steinberg, J. T. (2006). Linear prediction studies for the solar wind and Saturn kilometric radiation. *Annales Geophysicae*, 24, 3139–3150. <https://doi.org/10.5194/angeo-24-3139-2006>
- Thomas, B. T., & Smith, E. J. (1980). The parker spiral configuration of the interplanetary magnetic field between 1 and 8.5 AU. *Journal of Geophysical Research*, 85(A12), 6861–6867. <https://doi.org/10.1029/JA085iA12p06861>
- Trenchi, L., Marcucci, M. F., Palloccchia, G., Consolini, G., Bavassano Cattaneo, M. B., Di Lellis, A. M., et al. (2008). Occurrence of reconnection jets at the dayside magnetopause: Double Star observations. *Journal of Geophysical Research*, 113, A07S10. <https://doi.org/10.1029/2007JA012774>

- Treumann, R. A., & Baumjohann, W. (2020). Auroral kilometric radiation and electron pairing. *Frontiers in Physics*, 8(386). <https://doi.org/10.3389/fphy.2020.00386>
- Troshichev, O. A., & Andrezen, V. G. (1985). The relationship between interplanetary quantities and magnetic activity in the southern polar cap. *Planetary and Space Science*, 33(4), 415–419. [https://doi.org/10.1016/0032-0633\(85\)90086-8](https://doi.org/10.1016/0032-0633(85)90086-8)
- Von Rosenvinge, T. T., Barbier, L. M., Karsch, J., Liberman, R., Madden, M. P., Nolan, T., et al. (1995). The energetic particles: Acceleration, Composition, and Transport (EPACT) investigation on the Wind Spacecraft. *Space Science Reviews*, 71, 155–206. <https://doi.org/10.1007/BF00751329>
- Voots, G. R., Gurnett, D. A., & Akasofu, S. I. (1977). Auroral kilometric radiation as an indicator of auroral magnetic disturbances. *Journal of Geophysical Research*, 82(16). <https://doi.org/10.1029/JA082i016p02259>
- Wanliss, J. A., & Showalter, K. M. (2006). High-resolution global storm index: Dst versus SYM-H. *Journal of Geophysical Research*, 111, A02202. <https://doi.org/10.1029/2005JA011034>
- Waters, J. E., Cecconi, B., Bonnin, X., & Lamy, L. (2021). *Wind/waves flux density collection calibrated for auroral kilometric radiation*. version 1.0.
- Waters, J. E., Jackman, C. M., Lamy, L., Cecconi, B., Whiter, D., Bonnin, X., et al. (2021). Empirical selection of auroral kilometric radiation during a multipoint remote observation with wind and Cassini. *Journal of Geophysical Research: Space Physics*, 126, e2021JA029425. <https://doi.org/10.1029/2021JA029425>
- Weimer, D. R., & King, J. H. (2008). Improved calculations of interplanetary magnetic field phase front angles and propagation time delays. *Journal of Geophysical Research: Space Physics*, 113(A1). <https://doi.org/10.1029/2007JA012452>
- Weimer, D. R., Ober, D. M., Maynard, N. C., Burke, W. J., Collier, M. R., McComas, D. J., et al. (2002). Variable time delays in the propagation of the interplanetary magnetic field. *Journal of Geophysical Research*, 107(A8). <https://doi.org/10.1029/2001JA009102>
- Weimer, D. R., Ober, D. M., Maynard, N. C., Collier, M. R., McComas, D. J., Ness, N. F., et al. (2003). Predicting interplanetary magnetic field (IMF) propagation delay times using the minimum variance technique. *Journal of Geophysical Research*, 108(A1). <https://doi.org/10.1029/2002JA009405>
- Wilson, L. B., III, Brosius, A. L., Gopalswamy, N., Nieves-Chinchilla, T., Szabo, A., Hurley, K., et al. (2021). A quarter century of wind spacecraft discoveries. *Reviews of Geophysics*, 59, e2020RG000714. <https://doi.org/10.1029/2020RG000714>
- World Data Center for Geomagnetism Kyoto, Nose, M., Iyemori, T., Sugiura, M., & Kamei, T. (2015). *Geomagnetic AE index*. <https://doi.org/10.17593/15031-54800>
- Wu, C. S. (1985). Kinetic cyclotron and synchrotron maser instabilities: Radio emission processes by direct amplification of radiation. *Space Science Reviews*, 41, 215–298. <https://doi.org/10.1007/BF00190653>
- Wu, C. S., & Lee, L. C. (1979). A theory of the terrestrial kilometric radiation. *The Astrophysical Journal*, 230, 621–626. <https://doi.org/10.1086/157120>
- Xiao, F., Chen, L., Zheng, H., & Wang, S. (2007). A parametric ray tracing study of superluminous auroral kilometric radiation wave modes. *Journal of Geophysical Research*, 112, A10214. <https://doi.org/10.1029/2006JA012178>
- Yeoman, T. K., Lewis, R. V., Khan, H., Cowley, S. W. H., & Ruohoniemi, J. M. (2000). Interhemispheric observations of nightside ionospheric electric fields in response to IMF B_z and B_y changes and substorm pseudobreakup. *Annales Geophysicae*, 18, 897–907. <https://doi.org/10.1007/s00585-000-0897-x>
- Zhao, W., Liu, S., Zhang, S., Zhou, Q., Yang, C., & He, Y. (2019). Global occurrences of auroral kilometric radiation related to suprathermal electrons in radiation belts. *Geophysical Research Letters*, 46, 7230–7236. <https://doi.org/10.1029/2019GL083944>